

Numerical Heat Transfer, Part B: Fundamentals

An International Journal of Computation and Methodology

ISSN: 1040-7790 (Print) 1521-0626 (Online) Journal homepage: www.tandfonline.com/journals/unhb20

Magnetic feature and regression analysis of Reiner-Philippoff boundary layer flow

Yusuf O. Tijani, Shina D. Oloniju, Olumuyiwa Otegbeye & Ajiboye R. Babalola

To cite this article: Yusuf O. Tijani, Shina D. Oloniju, Olumuyiwa Otegbeye & Ajiboye R. Babalola (2025) Magnetic feature and regression analysis of Reiner-Philippoff boundary layer flow, Numerical Heat Transfer, Part B: Fundamentals, 86:3, 604-622, DOI: [10.1080/10407790.2023.2290189](https://doi.org/10.1080/10407790.2023.2290189)

To link to this article: <https://doi.org/10.1080/10407790.2023.2290189>



Published online: 11 Dec 2023.



Submit your article to this journal [↗](#)



Article views: 110



View related articles [↗](#)






View Crossmark data [↗](#)



Citing articles: 4 View citing articles [↗](#)



Magnetic feature and regression analysis of Reiner-Philippoff boundary layer flow

Yusuf O. Tijani^a , Shina D. Oloniju^b , Olumuyiwa Otegbeye^c , and
Ajiboye R. Babalola^d 

^aDepartment of Mathematics and Applied Mathematics, Nelson Mandela University, University Way, Gqeberha, South Africa; ^bDepartment of Mathematics, Rhodes University, Makhanda, Grahamstown, South Africa; ^cSchool of Computer Science and Applied Mathematics, University of Witwatersrand, Johannesburg, South Africa; ^dDepartment of Computational and Data Science, George Mason University, Incheon Global Community, Korea

ABSTRACT

The design and optimization of magnetic fluid-based processes, such as magnetohydrodynamic power generation and magnetic drug targeting, have become significant in recent times. To understand the magnetic and radiation features, as well as the sensitivity of engineering physical quantities to each dimensionless parameter in fluid flow, the Reiner-Philippoff (RP) fluid is best suited in this instance, as it exhibits shear-thickening, shear-thinning, and Newtonian behavior. The non-similar transformation is used to transform the partial differential equations that describe the flow into two-variable differential equations. The transformed dynamical equations are solved numerically using a spectral-based numerical technique; namely, the bivariate simple iteration method (BSIM). The effects of magnetic field strength and radiation parameter on the stretching and shrinking sheets are examined. The investigation reveals that both the magnetic field strength and radiation parameter have a significant impact on the flow behavior and rate of heat transfer. For the radiation parameter $R \in [0, 0.5]$, the skin friction coefficient and Nusselt number increase by 22.6% and 5.98%, respectively. Additionally, a 100% increment in Prandtl parameter reduces the Nusselt number by 287.36%. Regression analysis is performed to identify the most significant parameter affecting the engineering quantities. The results show that the Bingham constant, γ , is the only parameter that is not significant on the skin friction coefficient, while all the parameters have significant impact on the Nusselt number. The findings in this study have important implications in the biomedical industry, the design of machines, and the fourth industrial revolution.

ARTICLE HISTORY

Received 28 July 2023
Revised 31 October 2023
Accepted 17 November 2023

KEYWORDS

Boundary layer flow;
magnetic; radiation;
Reiner-Philippoff fluid

1. Introduction

The Reiner-Philippoff fluid is a class of non-Newtonian fluids that exhibit intriguing rheological behaviors. This class of fluid is typically characterized by its shear-thinning and viscoelastic properties. Shear-thinning refers to the property that the fluid's viscosity decreases with increasing shear rate. In other words, the fluid becomes less resistant to flowing as it is sheared more vigorously. Viscoelasticity, on the other hand, means that the fluid exhibits both viscous (fluid-like) and elastic (solid-like) behavior under deformation or stress. One way to understand the behavior

Nomenclature

<p>a stretching parameter</p> <p>c distance</p> <p>C_f skin friction coefficient</p> <p>c_p specific heat capacity</p> <p>f transformed dependent variable</p> <p>g transformed dependent variable</p> <p>k_1 mean absorption coefficient</p> <p>L length</p> <p>M magnetic parameter</p> <p>Nu Nusselt number</p> <p>Pr Prandtl number</p> <p>$P(\zeta)$ generalized main stream velocity function</p> <p>q_r radiative term</p> <p>q_w heat flux</p> <p>R radiation parameter</p> <p>Re Reynolds number</p> <p>T temperature of the fluid</p> <p>u velocity component in the x-axis</p> <p>u_e mainstream velocity</p> <p>v velocity component in the y-axis</p> <p>x, y Cartesian coordinates</p>	<p>γ Bingham constant</p> <p>θ transformed dependent variable</p> <p>κ thermal conductivity</p> <p>λ Reiner-Philippoff parameter</p> <p>ρ density</p> <p>ν kinematic viscosity</p> <p>μ dynamic viscosity</p> <p>σ^* Stefan–Boltzmann constant</p> <p>τ shearing stress</p> <p>ζ transformed independent variable</p> <p>η transformed independent variable</p> <p>ψ stream function</p> <p style="text-align: center;">Subscripts</p> <p>∞ condition at infinity in the y-axis</p> <p>o reference condition</p> <p>x local</p> <p>w wall</p>
---	--

of Reiner-Philippoff fluids is through the concept of “anomalous flow”. For Newtonian fluids, the relationship between shear stress and shear rate is linear (according to the equation $\tau = \mu \frac{du}{dy}$, where τ is shear stress, μ is viscosity, and $\frac{du}{dy}$ is shear rate). However, for Reiner-Philippoff fluids, the relationship is nonlinear, with the fluid’s viscosity depending on both the rate and history of deformation express nonlinearly as [1]

$$\mathcal{F}\left(\frac{\partial u}{\partial y}, \tau\right) = \frac{\partial u}{\partial y} - \frac{\tau}{\mu_\infty + \frac{\mu_o - \mu_\infty}{1 + \left(\frac{\tau}{\tau_o}\right)^2}} = 0. \quad (1)$$

Another notable feature of Reiner-Philippoff fluids is their thixotropic behavior. Thixotropy refers to the ability of a fluid to exhibit time-dependent changes in viscosity when subjected to deformation or stress. In other words, the viscosity of the fluid decreases over time after being subjected to shear stress, and slowly returns to its original value when the stress is removed. This property is desirable in applications such as coatings, adhesives, and lubricants, where the fluid should have a high viscosity at rest but be easy to apply or dispense when needed. Reiner-Philippoff fluids have a wide range of applications in various fields. For example, they are used as thickening agents in paints, inks, and cosmetics, as well as in drilling fluids and hydraulic fracturing fluids in petroleum engineering. They are also used in food processing, where they can be added to sauces, dressings, and spreads to improve stability and texture. Tijani et al. [2] investigated the impact of the magnetic dipole on the Reiner-Philippoff fluid. The heat transfer analysis over a Darcy-Forchheimer medium for a Reiner-Philippoff flow was studied by Kumar et al. [3]. Tijani et al [4] analyzed the impact of carbon nanotubes on Reiner-Philippoff boundary layer flow. To this end, the Reiner-Philippoff fluid is an important class of non-Newtonian fluids that exhibit unique rheological characteristics. Understanding their flow mechanics is crucial in many practical applications where viscosity and flow properties are important.

Magnetohydrodynamics (MHD) has been widely investigated by researchers due to its ubiquitous applications. Several MHD applications have their roots in physiology, such as the magnetic resonance imaging (MRI), magnetic devices in medication transferors, and the production of blood (biomagnetic fluid) due to the presence of hemoglobin molecules [5]. Mechanical and

electronic devices/systems such as dielectric grease, turbines, power station, missiles have paramount dependency on the study of magnetohydrodynamics. Hayat et al. [6] analyzed flow of a non-Newtonian fluid with non-orthogonal magnetic effect and non-constant thermal conductivity. Mabood et al. [7] probed the importance of magnetohydrodynamics on a nonlinearly radiating fluid flowing over an expanding surface. The study reported that the magnetic parameter has a linear relation with the skin drag force. Thammanna et al. [8] conducted a study on the unsteady stretching surface with chemical reaction involving a three-dimensional magnetohydrodynamic (MHD) flow of a couple stress Casson fluid. Prakasha et al. [9] discussed the thermal enhancement of aluminum nano-alloys in swirling aqueous MHD viscous nanofluid flow around a deformable cylinder. Several studies have been conducted to determine the significance of MHD in flow over an expanding or contracting surfaces, see [10–13]. Moreover, efforts on understanding the magneto-hydrodynamics effect on fluid flow in different geometry and medium have been investigated by various researchers, see [9, 14–16].

Regression analysis is a statistical technique employed to identify and understand the relationship between a dependent variable and one or more independent variables. This statistical methodology has practicable application in boundary layer flows by considering the relationship between the flow variables and the position within the boundary layer. The flow variables within the boundary layer, such as magnetic field, pressure or shear stress, as a function of distance from the expanding surface can be analyzed using regression technique. It helps mathematical modelers, researchers and engineers better understand the relationships between two or more interconnected variables. This importance cannot be overemphasized in the design of more efficient systems in machines, power turbines and electronic devices.

Researchers in the fields of science and engineering are increasingly turning to numerical analysis for solving differential equations. This trend is driven by the challenging nature of deterministic or stochastic differential equations, which might not be amenable to closed-form solutions due to their nonlinear nature. These methods include the finite difference method, the finite volume method, the spectral method, the homotopy analysis method, among many others. Employing several spectral-based methods for solving both differential and integral equations has significantly enhanced the efficiency with which a range of problems in science and engineering can be addressed. Through their research, Motsa et al. introduced several spectral-based numerical methods, including the spectral quasilinearization method, the spectral local linearization method (SLLM), and the spectral relaxation method (SRM) [17–20]. Ogunseye et al. [21] applied the SLLM in investigate the flow of an Eyring-Powell nanofluid in a channel with squeezing effect. Akolade and Tijani [22] comparatively studied the Casson and Williamson flow over an expanding Riga plate using the spectral quasilinearization method. Various research studies, as compiled here, have used the (bivariate) spectral local, quasi, and relaxation technique [23–26] to address several dynamical systems. For a thorough review of spectral-based methods applied to boundary layer problems, refer to the study conducted by Rai and Mondal [27]. To address the truncation error associated with Taylor series expansion, Otegbeye et al. [28] used a relaxation approach known as the bivariate simple iteration method. Their investigation focused on the unsteady flow of a Jeffrey fluid. The authors observed that the spectral-based method exhibited linear convergence and yielded highly accurate approximations even with a limited number of grid points.

To the authors' knowledge, no scientific research has explored the sensitivity and importance of individual parameters in the context of Reiner-Philippoff fluid flow over an expanding and/or contracting surface influenced by magnetic polarization and thermal radiation, using multivariable differential equations. The study aims to achieve several objectives: (i) modeling the 2D Reiner-Philippoff fluid over a contracting/expanding surface, (ii) transforming the governing dimensional PDEs into dimensionless systems through a non-similar group of transformations, (iii) applying the bivariate simple iteration method (BSIM) to the deterministic dynamical model, (iv)

investigating the behavior of relevant flow parameters through graphical analysis, and (v) using regression analysis to identify parameters influencing important engineering quantities.

2. Model formulation

Consider Reiner–Philippoff fluid depicted by a nonlinear shear-stress deformation function. The model is a three-parameter model which describes pseudoplasticity, dilatant and Newtonian characteristic, defined in Na [1] as

$$\frac{\partial u}{\partial y} = \frac{\tau}{\mu_\infty + \frac{\mu_0 - \mu_\infty}{1 + (\frac{\tau}{\tau_s})^2}}, \quad (2)$$

where τ is the shear stress, μ_∞ is the limiting viscosity, τ_s stands for reference shear stress and μ_0 is the zero shear viscosity.

This model delves into the two-dimensional flow of Reiner-Philippoff fluid over a sheet, considering the influence of magnetic effects and thermal radiation. The fluid's motion is influenced by the dynamics of the stretching and shrinking surface in the flow direction, with an arbitrary mainstream velocity u_e . Both the fluid and its medium are non-electrically conducting. A nonuniform, transverse magnetic field with strength $B(x) = B_0 x^{-\frac{1}{2}}$ acts in the flow direction. The temperature of the sheet, denoted as T_w , is lower than the ambient temperature T_∞ of the sheet, see Figure 1. The mass, momentum and energy conservation equations are similar to those outlined in a previous study by Na et al. [1].

$$\frac{\partial v}{\partial y} + \frac{\partial u}{\partial x} = 0, \quad (3)$$

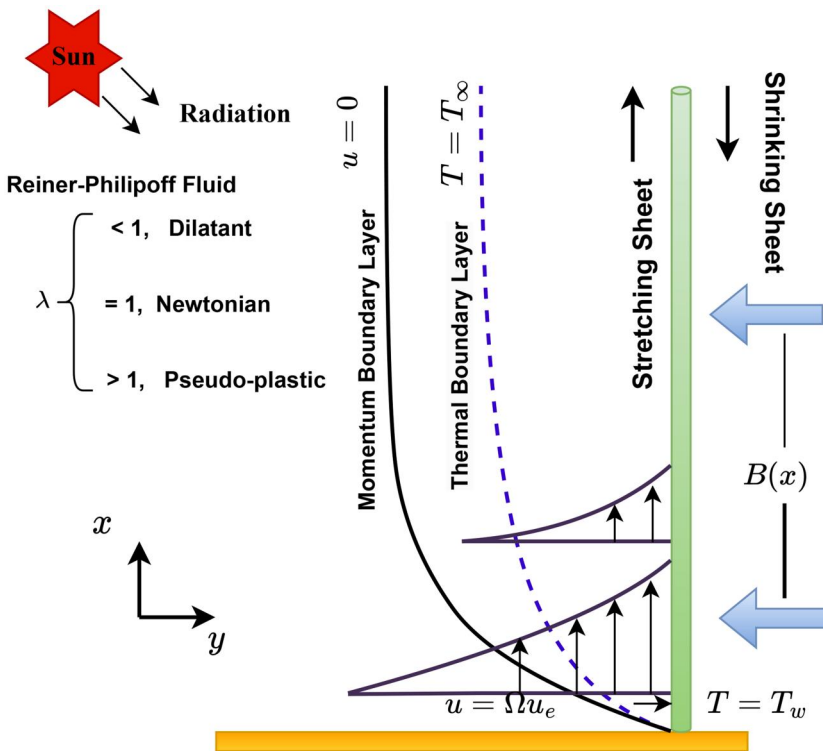


Figure 1. Flow configuration.

$$u_e \frac{du_e}{dx} + \frac{1}{\rho} \frac{\partial \tau}{\partial y} - \frac{\sigma B^2 u}{\rho} = u \frac{\partial u}{\partial x} + v \frac{\partial u}{\partial y}, \tag{4}$$

$$\frac{\kappa}{\rho c_p} \left(\frac{\partial^2 T}{\partial y^2} \right) - \frac{1}{\rho c_p} \frac{\partial q_r}{\partial y} = u \frac{\partial T}{\partial x} + v \frac{\partial T}{\partial y}. \tag{5}$$

The flow conditions at the wall and in the far-field are

$$\left. \begin{aligned} u(x, y) &= \Omega u_e, & v(x, y) &= v_e, & T(x, y) &= T_w & \text{as } y = 0, \\ u(x, y) &\rightarrow 0, & T(x, y) &\rightarrow T_\infty, & & & \text{as } y \rightarrow \infty. \end{aligned} \right\} \tag{6}$$

Here, u and v are the velocity components in x and y axes respectively, T represent the temperature of the fluid, ρ is the fluid density, c_p stands for the specific heat capacity of the fluid, κ is the thermal conductivity and u_e is the mainstream velocity. The linear radiative heat flux resulting from the Rosseland approximation is defined as

$$q_r = -\frac{4\sigma^*}{3k_1} \frac{\partial T^4}{\partial y} = -\frac{16\sigma^*}{3k_1} \left[T^3 \frac{\partial T}{\partial y} \right]. \tag{7}$$

Here, q_r represents the radiative term, k_1 denotes the mean absorption coefficient, and σ^* is the Stefan–Boltzmann constant.

2.1. Non-similar transformation

The following non-similar group of transformation, as outlined by Na [1], is used to transform Eqs. (3)–(5):

$$\zeta(x) = \tilde{x}, \quad \eta = \sqrt{\frac{u_e}{\tilde{x}\nu}} y, \quad f(\eta, \zeta) = \frac{\psi}{\sqrt{\tilde{x}u_e\nu}}, \quad \tau = \rho \sqrt{\frac{u_e^3}{\tilde{x}}} \nu g(\eta, \zeta), \quad \theta(\eta, \zeta) = \frac{T - T_\infty}{T_w - T_\infty}, \tag{8}$$

where

$$\tilde{x} = \frac{x}{L}, \quad u = u_e f'(\eta, \zeta) \quad \text{and} \tag{9}$$

$$v = -f'(\eta, \zeta) \left(\sqrt{u_e y} \frac{d\sqrt{u_e}}{dy} - \frac{u_e y}{2x} \right) - \sqrt{x\nu u_e} \frac{\partial f}{\partial \zeta} - \frac{\sqrt{\nu u_e}}{2\sqrt{x}} f(\eta, \zeta) - \frac{\sqrt{\nu x}}{2\sqrt{u_e}} f(\eta, \zeta) \frac{du_e}{d\zeta}.$$

Applying this transformation to the model in Eqs. (3)–(5) and the boundary conditions in Eq. (6), we derive the following set of differential equations:

$$\frac{g}{f''} = \frac{u_e^3 g^2 + \lambda \gamma^2 \zeta}{u_e^3 g^2 + \gamma^2 \zeta}, \tag{10}$$

$$g' + \frac{1 + P(\zeta)}{2} f f'' + P(\zeta)(1 - f^2) = \zeta \left(f' \frac{\partial f'}{\partial \zeta} - f'' \frac{\partial f}{\partial \zeta} \right) + M \zeta f', \tag{11}$$

$$\left(1 + \frac{4}{3} R \right) \theta'' = -\frac{1 + P(\zeta)}{2} Pr f \theta' + Pr \zeta \left(f' \frac{\partial \theta}{\partial \zeta} - \theta' \frac{\partial f}{\partial \zeta} \right). \tag{12}$$

Here, $P(\zeta) = \frac{\zeta}{u_e} \frac{du_e}{d\zeta}$, $\gamma = \frac{a\sqrt{a^3\nu}}{\tau_s}$ is the Bingham constant and $\lambda = \frac{\mu_o}{\mu_\infty}$ represents the Reiner–Philippoff fluid parameter, $Pr = \frac{c_p \nu}{\kappa}$ is the Prandtl number and $R = \frac{4\sigma^* T_\infty^3}{k_1 \kappa}$ stands for radiation parameter and $M = \frac{\sigma B_0^2 L}{\rho u_w}$ represent magnetic parameter. The dimensionless boundary conditions becomes

$$\begin{aligned} f'(\eta, \zeta) &= -\zeta n \frac{\partial f(\eta, \zeta)}{\partial \zeta} = \Omega, & f(\eta, \zeta) &= H, & \theta(\eta, \zeta) &= 1, & \text{at } \eta &= 0, \\ f'(\eta, \zeta) &\rightarrow 0, & \theta(\eta, \zeta) &\rightarrow 0, & \text{as } \eta &\rightarrow \infty. \end{aligned} \quad (13)$$

Note that $\Omega = 0$, $\Omega > 0$ and $\Omega < 0$ implies constant surface, stretching surface and contracting surface respectively. H is the constant mass flux, which takes three regional value of $H = 0$, $H > 0$ and $H < 0$ implies impermeable sheet, suction and injection, respectively.

The engineering physical parameters of interest, namely the surface drag (skin friction) coefficient and Nusselt number, are defined as follows:

$$C_f = \frac{\tau_w}{0.5\rho u_w^2}, \quad Nu_x = \frac{xq_w}{\kappa(T_w - T_\infty)}, \quad (14)$$

where the shear stress and surface heat flux, τ_w and q_w , are, respectively, defined as

$$\tau_w = \rho\sqrt{a^3\nu}g(\eta), \quad q_w = -\kappa\frac{\partial T}{\partial y}\Big|_{y=0} - q_r. \quad (15)$$

In dimensionless form, Eq. (14) using the definition defined in Eq. (15) becomes

$$\frac{1}{2}Re_x^{\frac{1}{2}}C_f = g(0, \zeta), \quad Re_x^{-\frac{1}{2}}Nu_x = -\left(1 + \frac{4}{3}R\right)\theta'(0, \zeta), \quad (16)$$

where $Re_x = \frac{u_\infty L}{\nu}$ is the Reynolds number.

3. Bivariate simple iteration method

In this section, we apply the bivariate simple iteration method to the system of Equations (10) – (12) and the corresponding boundary condition (13). The bivariate simple iteration method (BSIM), as introduced by Otegbeye et al. [28], leverages the underlying principle of fixed point methods in application to solving nonlinear differential equations [29]. Recall, from the fixed point method, that given

$$f(x) = 0, \quad (17)$$

we can derive an x such that another function $g(x)$ is introduced, resulting in

$$f(x) = x - g(x) = 0, \quad \text{or } f(x) = g(x) - x = 0. \quad (18)$$

Both forms presented in Eq. (18) lead to the recursive formula

$$x_{r+1} = g(x_r). \quad (19)$$

In this formulation, x_{r+1} is determined using the solution at x_r obtained from the function $g(x_r)$. In a similar manner, given the equation

$$\frac{g}{f''} = \frac{u_e^3 g^2 + \lambda \gamma^2 \zeta}{u_e^3 g^2 + \gamma^2 \zeta}, \quad (20)$$

we formulate a recursive scheme using a relaxation approach with the following rules:

- Express the nonlinear terms of g with an exponent greater than 1 at both the current and previous iteration levels in the form

$$g^n \approx g_r^{n-1} g_{r+1},$$

where subscripts r and $r + 1$ represent the previous and current iteration levels, respectively.

- Evaluate nonlinear terms of other functions at the previous iteration level.

Therefore, based on the set rules, the linear form of Eq. (20) is obtained

$$\mathbf{A}_1 g_{r+1} = \mathbf{B}_{1,r}, \tag{21}$$

where

$$\mathbf{A}_1 = u_e^3 g_r^2 + \gamma^2 \zeta - u_e^3 f''_r g_r, \quad \mathbf{B}_{1,r} = \lambda \gamma^2 \zeta f''_r.$$

Typically, the BSIM (or Gauss-Seidel type methods in general) requires using the updated solution of g in subsequent equations. However, due to the absence of boundary conditions associated with Eq. (20), we directly differentiate g to represent g' in Eq. (11), resulting in the following linearized equation:

$$[b_{0r}] f'''_{r+1} + [b_{1r}] f''_{r+1} + [b_{2r}] f'_{r+1} + [b_{3r}] f_{r+1} - [b_{4r}] \frac{\partial f'_{r+1}}{\partial \zeta} + [b_{5r}] \frac{\partial f_{r+1}}{\partial \zeta} = \mathbf{B}_{2,r}. \tag{22}$$

where terms in [...] represent vector quantities and

$$\begin{aligned} b_{0r} &= u_e^3 g_{r+1}^2 + \frac{\lambda \gamma^2 \zeta}{u_e^3 g_{r+1}^2 + \gamma^2 \zeta}, & b_{1r} &= \frac{1 + P(\zeta)}{2} f_r + \zeta \frac{\partial f_{r+1}}{\partial \zeta} + \frac{2u_e^3 g_{r+1} g'_{r+1} \zeta \gamma^2 (1 - \lambda)}{u_e^3 g_{r+1}^2 + (\gamma^2 \zeta)^2}, \\ b_{2r} &= -2P(\zeta) f'_r - \zeta \frac{\partial f'_r}{\partial \zeta} - M\zeta, & b_{3r} &= \frac{1 + P(\zeta)}{2} f''_r, & b_{4r} &= \zeta f'_r, \\ b_{5r} &= \zeta f'_r, & \mathbf{B}_{2,r} &= \frac{1 + P(\zeta)}{2} f_r f_r^2 - P(\zeta) - P(\zeta) f'_r 2 - \zeta f'_r \frac{\partial f'_r}{\partial \zeta} + \zeta f_r^2 \frac{\partial f_r}{\partial \zeta}. \end{aligned}$$

Likewise, the updated solutions to f and its corresponding derivatives are employed in the relaxed form of Eq. (12), leading to the following equation

$$c_{0r} \theta''_{r+1} + [c_{1r}] \theta'_{r+1} - [c_{2r}] \frac{\partial \theta_{r+1}}{\partial \zeta} = \mathbf{0}, \tag{23}$$

where

$$c_{0r} = 1 + \frac{4R}{3}, \quad c_{1r} = \frac{1 + P(\zeta)}{2} Pr f_{r+1} + Pr \zeta \frac{\partial f_{r+1}}{\partial \zeta}, \quad c_{2r} = Pr \zeta f'_{r+1}.$$

The decoupled system of linear Eqs. (21)–(23) is solved using the Chebyshev spectral collocation method. This numerical method approximates a function through a linear combination of the Lagrange interpolating polynomials, and explicitly expressed the derivative of the function by differentiating the Lagrange polynomials, evaluated at the Chebyshev-Gauss-Lobatto nodes [30]. It is worth noting that an arbitrary domain $[a, b]$ is mapped onto the computational domain $[-1, 1]$. Trefethen [30] has provided in-depth details about the method. Consequently, to approximate the solutions $g(\eta, \zeta), f(\eta, \zeta)$, and $\theta(\eta, \zeta)$ of Eqs. (21)–(23), we assume the following forms:

$$\left. \begin{aligned} g(\eta, \zeta) &= \sum_{i=0}^{N_\eta} \sum_{j=0}^{N_\zeta} g(\eta_i, \zeta_j) L_i(\eta) L_j(\zeta), \\ f(\eta, \zeta) &= \sum_{i=0}^{N_\eta} \sum_{j=0}^{N_\zeta} f(\eta_i, \zeta_j) L_i(\eta) L_j(\zeta), \\ \theta(\eta, \zeta) &= \sum_{i=0}^{N_\eta} \sum_{j=0}^{N_\zeta} \theta(\eta_i, \zeta_j) L_i(\eta) L_j(\zeta), \end{aligned} \right\} \tag{24}$$

where L_i and L_j are the Lagrange cardinal functions defined as

$$L_i(\eta) = \prod_{i=0, i \neq k}^{N_\eta} \frac{\eta - \eta_k}{\eta_i - \eta_k}, \quad L_j(\zeta) = \prod_{j=0, j \neq k}^{N_\zeta} \frac{\zeta - \zeta_k}{\zeta_j - \zeta_k},$$

where

$$L_i(\eta_k) = \delta_{ik} = \begin{cases} 0 & \text{if } i \neq k \\ 1 & \text{if } i = k \end{cases}, \quad L_j(\zeta_k) = \delta_{jk} = \begin{cases} 0 & \text{if } j \neq k \\ 1 & \text{if } j = k \end{cases}.$$

We discretize the domain at the Chebyshev-Gauss-Lobatto points, η_i and ζ_j , and these points are defined as follows:

$$\eta_i = \cos \frac{\pi i}{N_\eta}, \quad i = 0, 1, \dots, N_\eta, \quad \zeta_j = \cos \frac{\pi j}{N_\zeta}, \quad j = 0, 1, \dots, N_\zeta. \quad (25)$$

The solutions of the flow model are approximated using Eq. (24); however, the derivatives of the functions are represented differently. To illustrate, let us consider a simple case of using two grid points in space, implying the points to be considered are $\{\eta_0 = -1, \eta_1 = 1\}$. We then have an approximate solution in terms of first degree Lagrange polynomial

$$P_1(\eta) \approx f(\eta) = \frac{\eta - \eta_1}{\eta_0 - \eta_1} f(\eta_0) + \frac{\eta - \eta_0}{\eta_1 - \eta_0} f(\eta_1). \quad (26)$$

which reduces to

$$P_1(\eta) \approx f(\eta) = -\frac{1}{2}(\eta - 1)f(\eta_0) + \frac{1}{2}(\eta + 1)f(\eta_1). \quad (27)$$

To evaluate the first derivative of f , we differentiate Eq. (27) with respect to η to obtain

$$f'(\eta) = -\frac{1}{2}f(\eta_0) + \frac{1}{2}f(\eta_1), \quad (28)$$

which is then represented in matrix-vector form as

$$\begin{bmatrix} -\frac{1}{2} & \frac{1}{2} \\ -\frac{1}{2} & \frac{1}{2} \end{bmatrix} \begin{bmatrix} f(\eta_0) \\ f(\eta_1) \end{bmatrix} = \begin{bmatrix} f'(\eta_0) \\ f'(\eta_1) \end{bmatrix}. \quad (29)$$

Here, the coefficient matrix is the **differentiation matrix**. For a more in-depth understanding of the development of the differentiation matrix, see Trefethen [30], which provides comprehensive details on both the derivation and implementation. In a broad sense, differentiation matrices (denoted as \mathbf{D} in space and d in time) are used to evaluate the derivatives as

$$\begin{aligned} \left. \frac{\partial f^{(p)}}{\partial \eta^{(p)}} \right|_{\eta_i, \zeta_j} &= \mathbf{D}^{(p)} \mathbf{F}_i, & \left. \frac{\partial f}{\partial \zeta} \right|_{\eta_i, \zeta_j} &= \sum_{j=0}^{M_\zeta} d_{ij} \mathbf{F}_j, \\ \left. \frac{\partial \theta^{(p)}}{\partial \eta^{(p)}} \right|_{\eta_i, \zeta_j} &= \mathbf{D}^{(p)} \mathbf{\Theta}_i, & \left. \frac{\partial \theta}{\partial \zeta} \right|_{\eta_i, \zeta_j} &= \sum_{j=0}^{M_\zeta} d_{ij} \mathbf{\Theta}_j. \end{aligned}$$

By applying these representations to the decoupled system of Eqs. (21)–(23), we obtain

$$\left[\mathbf{A}_{1,r,i} \right] \mathbf{G}_{r+1,i} = \mathbf{B}_{1,r,i} \quad (30)$$

$$\left[\mathbf{b}_{0,r,i} \mathbf{D}^3 + \mathbf{b}_{1,r,i} \mathbf{D}^2 + \mathbf{b}_{2,r,i} \mathbf{D} + \mathbf{b}_{3,r,i} - \mathbf{b}_{4,r,i} \sum_{j=0}^{M_\zeta-1} \mathbf{D} d_{i,j} + \mathbf{b}_{5,r,i} \sum_{j=0}^{M_\zeta-1} d_{i,j} \right] \mathbf{F}_{r+1,i} = \mathbf{B}_{2,r,i} \tag{31}$$

$$\left[c_{0,r} \mathbf{D}^2 + [c_{1,r,i} \mathbf{D} - [c_{2,r,i} \sum_{j=0}^{M_\zeta-1} d_{i,j}]] \right] \Theta_{r+1,i} = \mathbf{B}_{3,r,i} \tag{32}$$

where

$$\begin{aligned} \mathbf{B}_{2,r,i} &= [\mathbf{b}_{4,r,i} d_{i,M_\zeta} (\mathbf{D} \mathbf{F}_{M_\zeta}) - [\mathbf{b}_{5,r,i} d_{i,M_\zeta} (\mathbf{F}_{M_\zeta})] + \mathbf{B}_{2,r}, \\ \mathbf{B}_{3,r,i} &= [c_{2,r,i} d_{i,M_\zeta} \Theta_{M_\zeta} + \mathbf{0}. \end{aligned}$$

To assess the accuracy and efficiency of the bivariate simple iteration method used in this study, we present the norms of the residual and convergence errors at $\zeta = 0.5$ and $\zeta = 1$. The residual error measures how precisely the approximate solutions solves the system of nonlinear differential equations subject to the provided boundary conditions. Conversely, the convergence error norm quantifies how rapidly the iterative scheme converges. We define the convergence error norms as follows: $\|G\|_\infty = \|\mathbf{G}_{r+1} - \mathbf{G}_r\|_\infty$, $\|F\|_\infty = \|\mathbf{F}_{r+1} - \mathbf{F}_r\|_\infty$ and $\|\Theta\|_\infty = \|\Theta_{r+1} - \Theta_r\|_\infty$. These results are depicted in Figures 2 and 3. The convergence error norms reveal that the iterative scheme exhibits a quadratic rate of convergence. In both sets of figures, the error norms fall

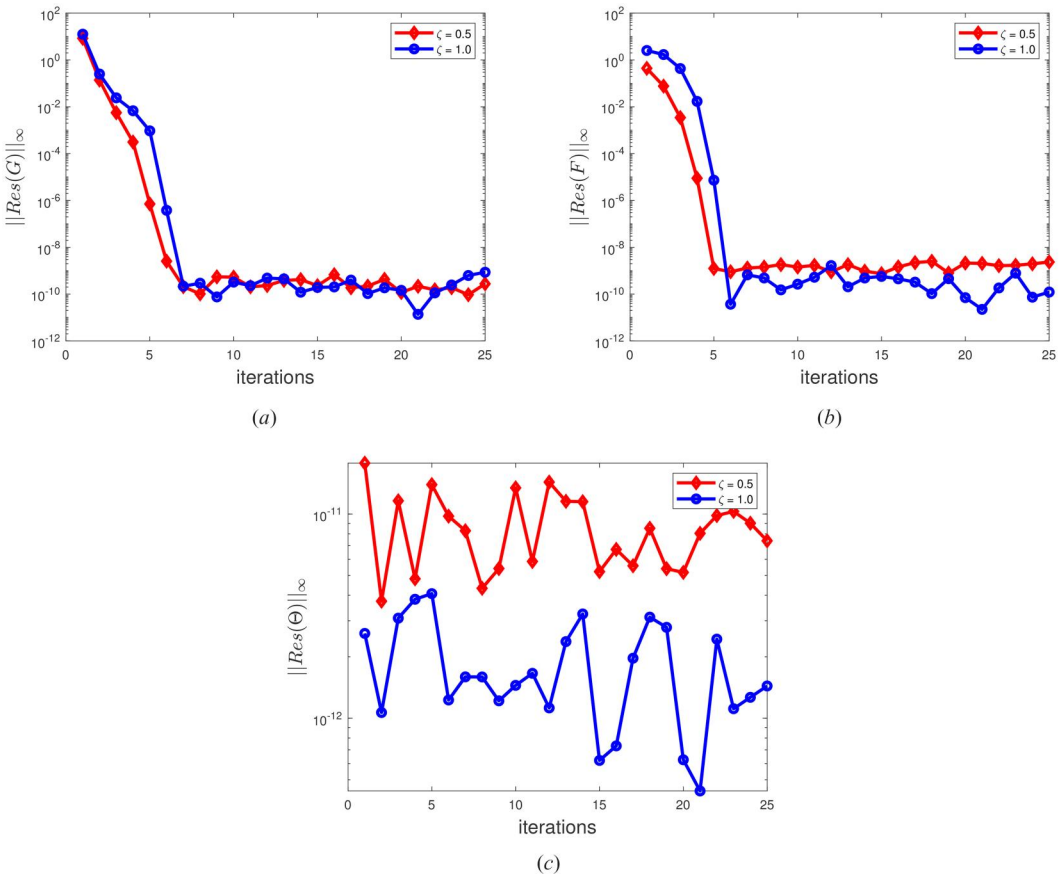


Figure 2. Norms of the residual error for Eqs. (10)–(12).

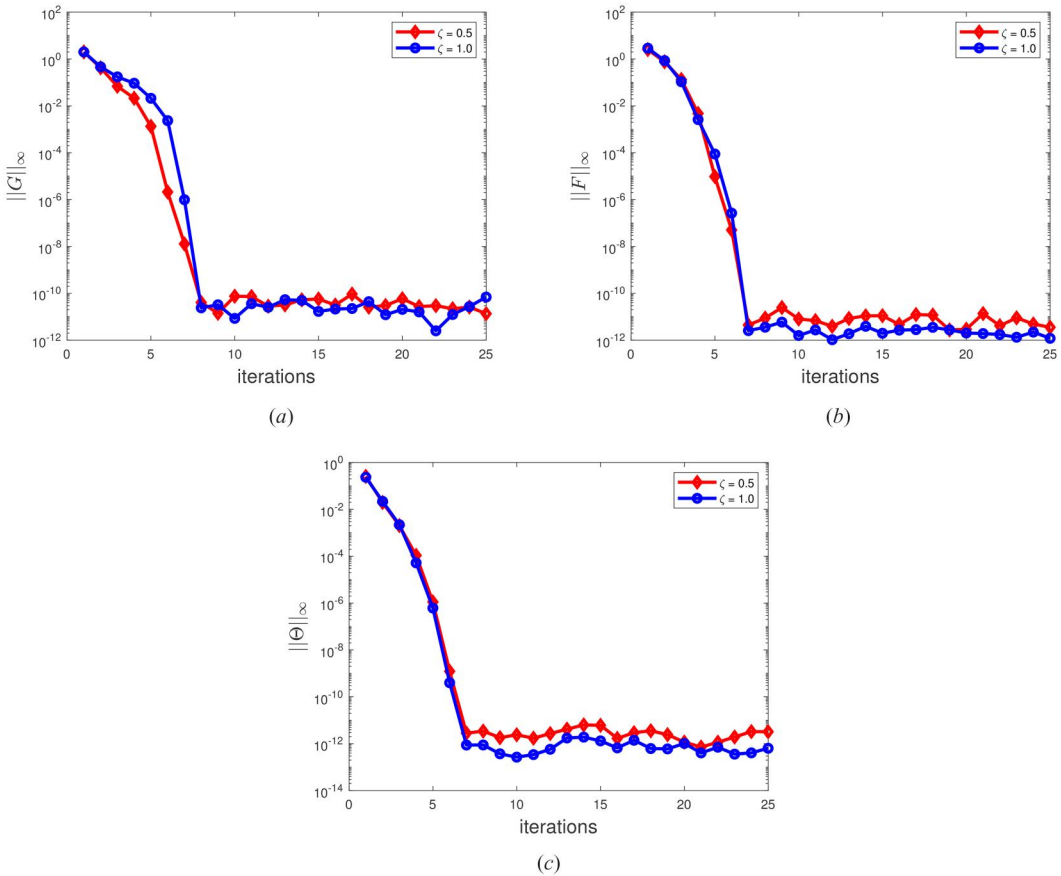


Figure 3. Norms of the convergence errors of the approximate solution G, F and Θ .

within the range of $[10^{-14}, 10^{-10}]$ after the 25th iteration, confirming the accuracy and convergence of the spectral-based iterative method used in this study.

4. Results and discussion

In this section, we present and discuss the results obtained using the bivariate simple iteration scheme (30)–(32). The simulation used the parametric value of $Pr = 0.7$, $M = 0.3$, $R = 0.1$, $\lambda = 1.0$, $\gamma = 0.5$, $H = 0.1$, $\Omega = 1.0$ (stretching sheet) and $\Omega = -1.0$ (shrinking sheet) as default unless otherwise stated. Before discussing the importance of the flow parameter, it is worth mentioning that $\lambda < 1$ represent shear-thickening fluid, $\lambda = 1$ is Newtonian fluid and $\lambda > 1$ stands for shear-thinning fluid. The Bingham constant γ is a crucial parameter used to characterize the behavior of specific non-Newtonian fluids. The Bingham constant signifies the slope of the shear stress-shear rate relationship within the fluid flow region. In Figure 4, the behavior of the skin friction and heat transfer coefficient against λ is illustrated, considering three different slopes of the shear stress-shear rate relationship denoted by γ . Notably, $\lambda = 1$ emerges as a turning point for both the wall's frictional force and heat transfer coefficient.

In Figure 5, the behavior of the skin friction and Nusselt number for the Reiner-Philippoff fluid is depicted with $\gamma \in [0.0, 2.0]$ for three distinct λ values. Notably, the surface's wall frictional force for shear-thickening fluid increases with the ascent of the Bingham constant. The Newtonian fluid demonstrates a constant skin friction and Nusselt number across the range of γ .

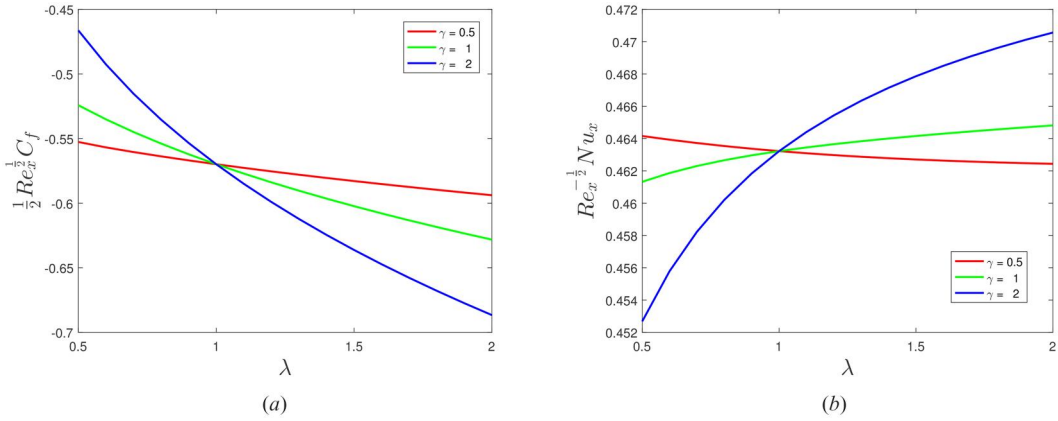


Figure 4. Skin friction and Nusselt number against λ for various values of γ .

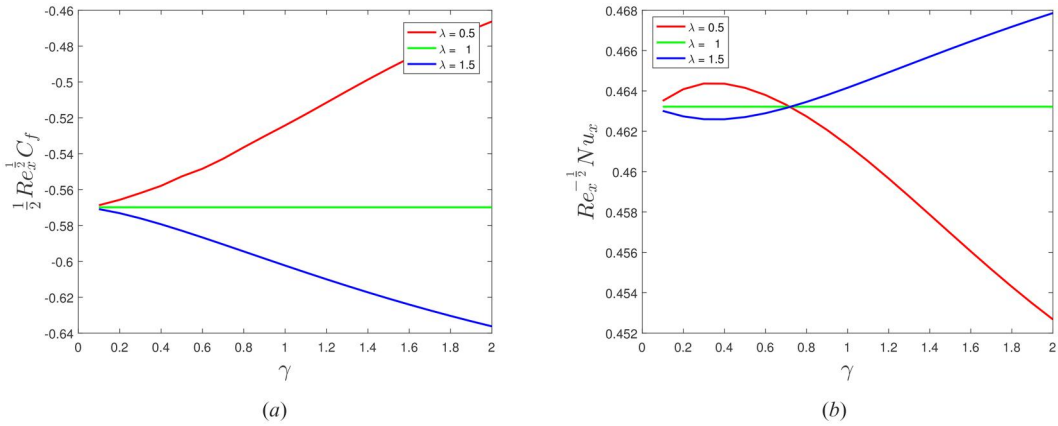


Figure 5. Skin friction and Nusselt number against γ for various values of λ .

As for the shear-thickening fluid, it exhibits an increasing rate of heat transfer until reaching a turning point in the vicinity of $\gamma = 0.75$, after which it decreases. Conversely, the behavior of the shear-thinning fluid contrasts with that of the shear-thickening fluid. In Figure 6, the impact of mass flux on friction drag coefficient and Nusselt number is elucidated. Suction is observed to diminish the fluid velocity near the wall, creating a region with lower velocity gradients. Consequently, the velocity gradient (shear) between the fluid near the wall and the rest of the flow decreases. This reduction in velocity gradient results in a decrease in the wall shear stress as the suction rate increases. Additionally, it is noted that the shear-thinning fluid exhibits the lowest skin friction coefficient. The influence of H on the rate of heat transfer is relatively negligible. This is unsurprising since H primarily affects the flow behavior through the wall boundary condition in the momentum equation.

The influence of the magnetic parameter M is illustrated in Figure 7. The dotted lines represent the shrinking sheet ($\Omega = -1.0$), while the solid lines are for the stretching sheet ($\Omega = 1.0$). It is evident that as the magnetic parameter increases, the fluid's motion on the stretched sheet diminishes. This reduction is attributed to the magnetic force acting as a constraint throughout the fluid flow, leading to an increased frictional structure as M increases. However, the magnetic

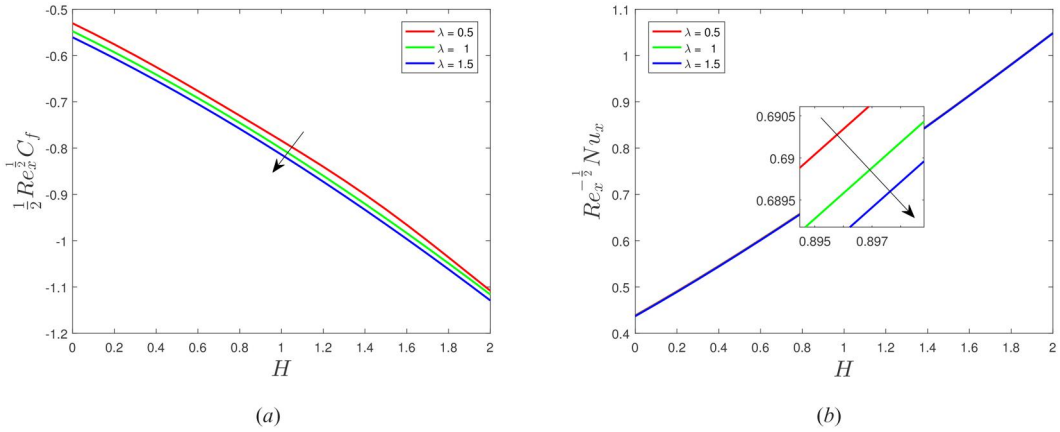


Figure 6. Skin friction and Nusselt number against H for various values of λ .

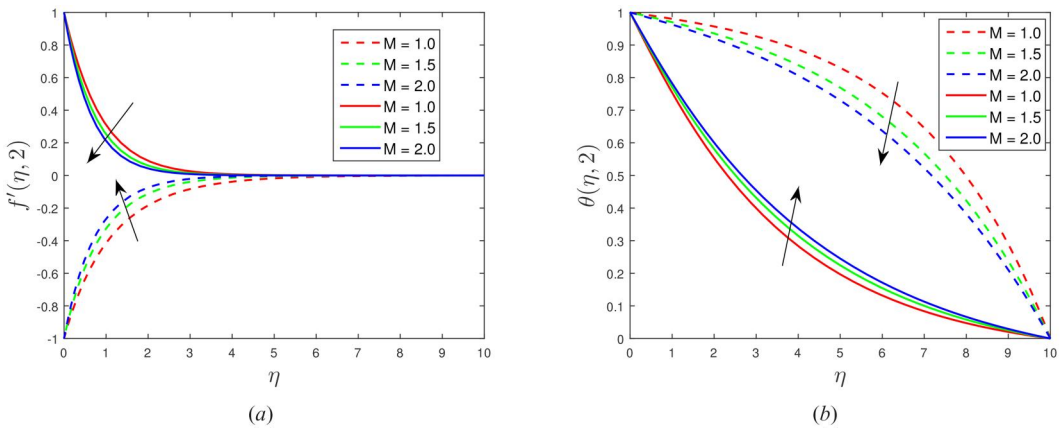


Figure 7. Velocity and temperature profiles against η for various values of M .

parameter enhances fluid flow over the shrinking sheet. As the shrinking sheet contracts, the magnetic force, which opposes fluid movement on the stretched sheet, indirectly acts as a driving force supporting fluid movement on the shrinking sheet. The impact of thermal radiation and the Prandtl number is vividly illustrated in Figure 8 for both expanding and contracting sheets. It is observed that an increase in Pr leads to a decrease in the temperature profile for the stretching sheet, while an increase in Pr enhances the temperature distribution in the flow over the shrinking sheet. This behavior is a result of the Prandtl number being strongly dependent on the thermal diffusivity of the fluid, meaning that a larger Pr corresponds to a weaker thermal diffusivity. The radiation parameter R supports the temperature profile in the stretching sheet by directly influencing the energy exchange between the fluid and its surroundings. Nevertheless, it is evident that an increase in the radiation number R diminishes the temperature distribution in the flow on the shrinking sheet. Overall, an increase in the radiation parameter R induces alterations in fluid properties and consequently influences the temperature gradient within the flow.

In Figure 9, the simultaneous impact of the radiation parameter R and the Prandtl number Pr on $Re_x^{-1/2} Nu_x$ is depicted. It can be inferred that increasing the radiation parameter enhances the rate of heat transfer positively. Furthermore, fluids with higher Prandtl numbers exhibit an enhanced heat transfer rate compared to fluids with lower Prandtl numbers. The impact of streamwise location or point ζ and fluid parameter λ on the skin drag force and Nusselt number

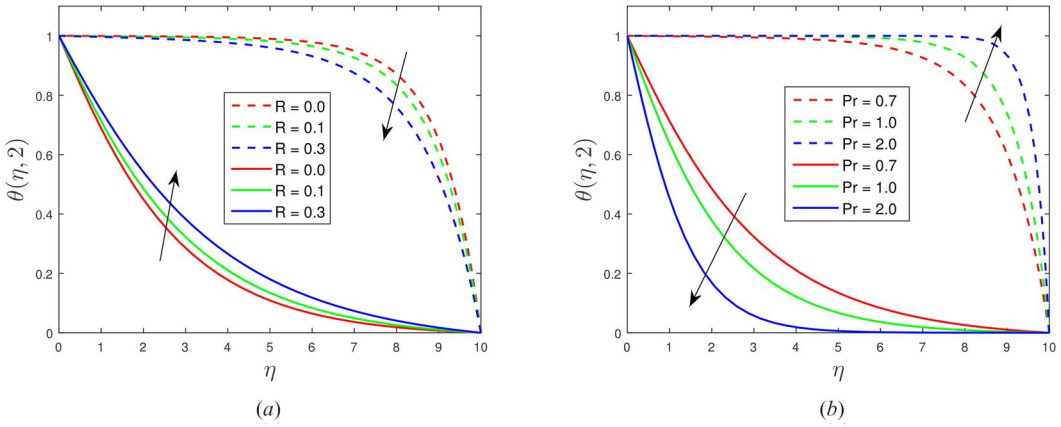


Figure 8. Temperature profiles against η for various values of R and Pr .

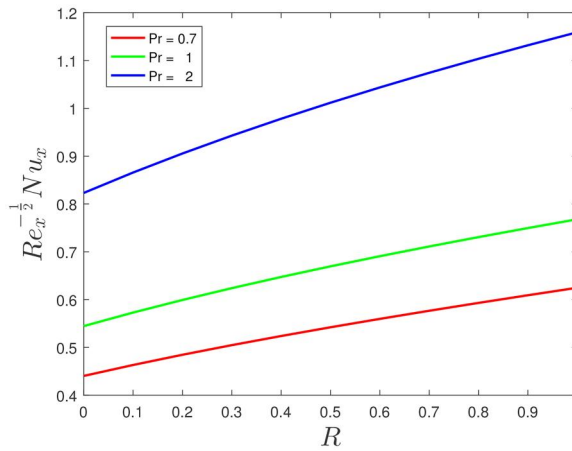


Figure 9. Nusselt number against R for various values of Pr .

profile is presented in Figure 10. It is observed that a higher ζ increases the friction drag force and Nusselt number. For $\zeta = 0$, the skin drag force for shear-thinning, shear-thickening, and Newtonian fluids is the same. However, at $\zeta = 1$, it is noted that the skin friction of dilatant fluid is greater compared to Newtonian fluid, while the shear-thinning fluid has the least skin drag force. The implication is that the self-similar solution, which corresponds to $\zeta = 0$, is not advisable to achieve the best heat transfer rate and wall shear stress. These are more effectively attained at considerably high ζ . Hence, nonsimilar transformation is recommended for this kind of problem. This is most preferable especially when dealing with flow problems that exhibit significant variations in the flow field or boundary conditions. These variations may occur due to factors such as changes in geometry, boundary conditions, or physical properties.

5. Regression analysis

Regression analysis finds applications in various fields, such as manufacturing industries, population modeling, and forecasting. With this in mind, in this section, we develop a quadratic regression model to perform statistical analysis on the skin friction coefficient and Nusselt number. To this end, a set of 200 values of Pr randomly selected in the interval $[0.7, 40.0]$, $M \in [0.2, 5.0]$, $R \in$

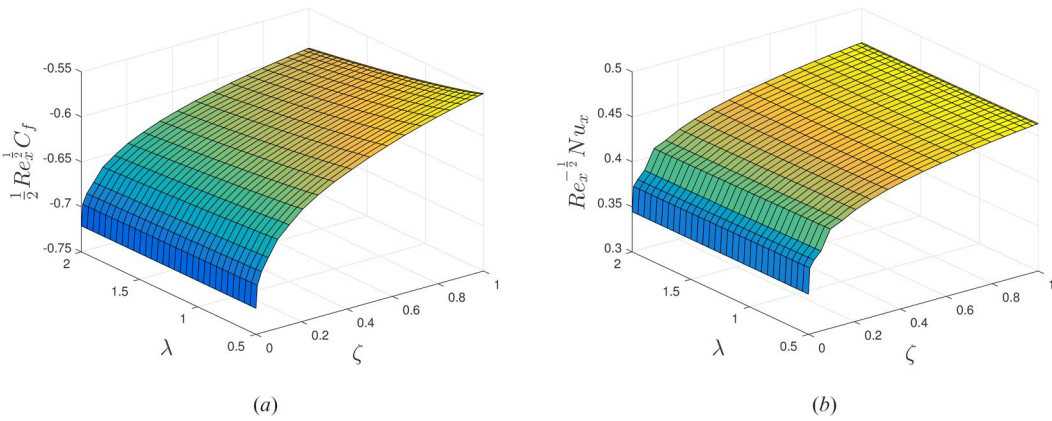


Figure 10. Skin friction and Nusselt number against λ and streamwise location ζ .

$[0.1, 4.0]$, $H \in [0.0, 2.0]$, $\Omega \in [0.6, 1.0]$ and $\gamma \in [0.5, 2.0]$ to estimate $\frac{1}{2}Re_x^{\frac{1}{2}}C_f$ and $Re_x^{-\frac{1}{2}}Nu_x$ for various Reiner-Philippoff fluid parameter $\lambda \in [0.0, 1.5]$. The parameter range is more significant for λ to cover the range of both shear-thinning fluid and shear-thickening fluid. This is also corroborated by the range of Pr , which covers fluids in this range. For example, the Pr for water is around 6.9, while for gases it falls in the neighborhood of 0.7.

The regression estimation for the Nusselt and skin-friction follows the mathematical expression given as

$$\left. \begin{aligned} \frac{1}{2}Re_x^{\frac{1}{2}}C_{f_{est}} &= \frac{1}{2}Re_x^{\frac{1}{2}}C_f + \beta_1\gamma + \beta_2M + \beta_3R + \beta_4Pr + \beta_5\Omega + \beta_6H + \beta_7\lambda. \\ Re_x^{-\frac{1}{2}}Nu_{x_{est}} &= Re_x^{-\frac{1}{2}}Nu_x + \beta_8\gamma + \beta_9M + \beta_{10}R + \beta_{11}Pr + \beta_{12}\Omega + \beta_{13}H + \beta_{14}\lambda. \end{aligned} \right\} \quad (33)$$

Here, $\beta_1, \beta_2, \beta_3, \dots, \beta_{14}$ are the regression coefficients. It is immediate to see that when all the parameters are zero, we obtain $\frac{1}{2}Re_x^{\frac{1}{2}}C_{f_{est}} = \frac{1}{2}Re_x^{\frac{1}{2}}C_f$ and $Re_x^{-\frac{1}{2}}Nu_{x_{est}} = Re_x^{-\frac{1}{2}}Nu_x$. Therefore, the regression terms (representing unknown parameters) have a substantial impact on both response parameters, i.e. Nusselt number and skin friction.

It is important to note that the process of finding a mathematical relationship for which this study intends to achieve for the local Nusselt or the skin friction coefficient with all the seven independent variables as expressed in Eq. (33) is in line with the theory of statistical inference and as such, it is reasonable to construct a statistical procedure. This is consequent on defining a null hypothesis H_0 : that the parameters β_i 's expressed in Eq. (33) are equal and equal to zero. On the alternative hypothesis H_a : there is a contradiction of at least one of the β 's; that is one of them is different and different from zero.

Figure 11 is the regression analysis graph. It depicts the strength of relationship, residuals and line of best fit. Table 1 presents the analysis of variance (ANOVA) to establish the relationship between the Nusselt Number and skin friction with the independent variables in the flow equations. According to ANOVA results, the F-value serves as an indicator of the information resulting from the pivotal approximation between the model and other components embedded in it. On the other hand, the p-value validates the reliability of the demonstration from a statistical point of view. The F-value in itself can replace the p-value but in this sense, it would require the F distribution table to do so. A high F-value indicates significance in the outcome, while a low p-value strongly supports the significance claimed by the F-value. Consequently, we can say that both the F-value and the p-value complement each other and play a crucial role in the analysis.

In details, definition of terms for the regression analysis is as follows, for the regression model, there are two components; they are the deterministic and the stochastic components. The stochastic component which is the error component has points which are not captured by regression

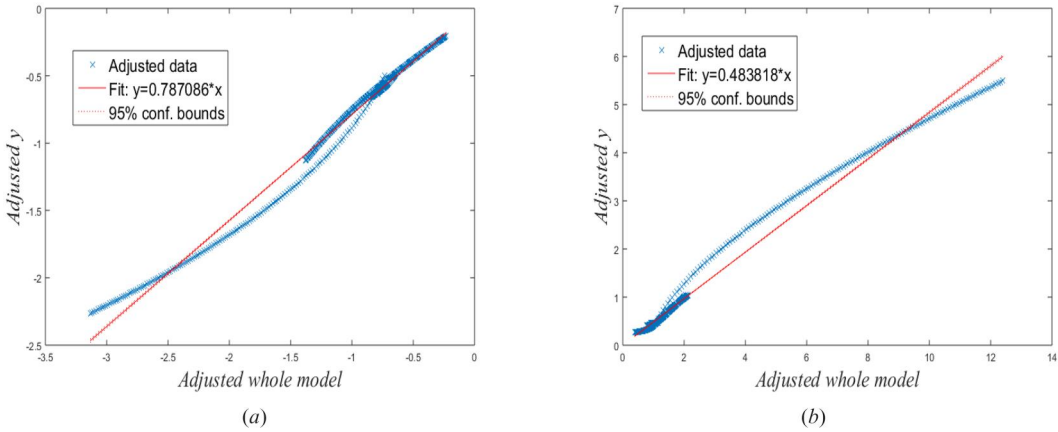


Figure 11. Graph of the regression equation for skin friction and Nusselt number.

Table 1. Analysis of variance for the skin friction and Nusselt number.

Source	Skin friction (SF)					Nusselt number (NN)				
	DF	Adj SS	Adj MS	F-Value	p-Value	DF	Adj SS	Adj MS	F-Value	p-Value
Regression	7	175.159	25.023	11314.31	0.000	7	1361.43	194.49	12064.14	0.000
γ	1	0.002	0.002	1.030	0.311	1	0.32	0.32	19.63	0.000
M	1	129.097	129.097	58372.89	0.000	1	4.36	4.36	270.27	0.000
R	1	0.088	0.088	39.79	0.000	1	9.72	9.72	602.86	0.000
Pr	1	0.088	0.088	39.79	0.000	1	1144.64	1144.64	71001.63	0.000
Ω	1	7.173	7.173	3243.19	0.000	1	0.91	0.91	56.41	0.000
H	1	8.188	8.188	3702.48	0.000	1	8.19	8.19	507.89	0.000
λ	1	0.376	0.376	169.99	0.000	1	0.16	0.16	9.62	0.002
Error	1049	2.320	0.002			1049	16.91	0.02		
Lack of fit	1045	2.319	0.002	7.75	0.028	1045	16.91	0.02	7088.78	0.000
Pure error	4	0.001	0.000			4	0.00	0.00		
Total	1056	177.478				1056	1378.35			

line, and they are cumulative of the lack of fit and the pure error. The lack of fit tends to tell how good the model is in relation to the data from the independent and response variable and when the lack of fit is large, it tells that the model neglects the true picture of the functional connectedness between the independent variable and its dependent variable.

Figure 12 shows a normal quantile-quantile residual plot for both the skin friction and the Nusselt number, exhibiting a long and steep tail. The long and steep tail is displayed in the histogram chart displayed in Figure 13.

Figure 12 shows a straight line for both normal probability plot of residual signifying the errors are normally distributed and a staying end to opposite directions. By implication, the regression model fits well but with a little effort based on the complexity of the model. The regression coefficients for both responses (skin friction coefficient and the Nusselt Number) with its related p-value for nonlinear polynomial model are shown in Table 3. It is good to note that a p-value higher than the conventional p-value (of either 0.05 or 0.01; depending on which is considered) is regarded as statistically insignificant, by implication no relative change can be noted on the output consequent from what might have happened in the input. On the other hand, one might take extra care as to also consider the situation when p-value is less than or equal to the level of significance so one does not commit the grave type II error. The mathematical representation for Table 1 and value for the corresponding regression coefficients in Eq. (33) is given as

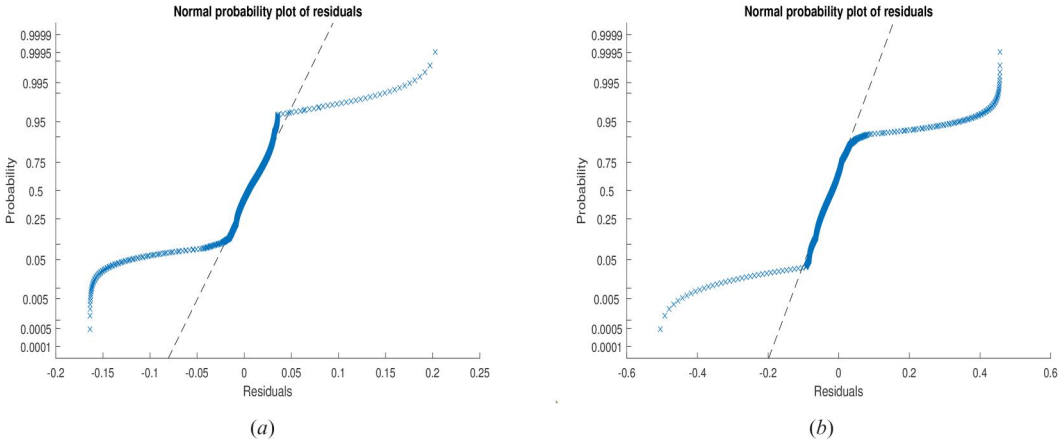


Figure 12. Normal probability plot of residual for skin friction and Nusselt number for analysis of variance.

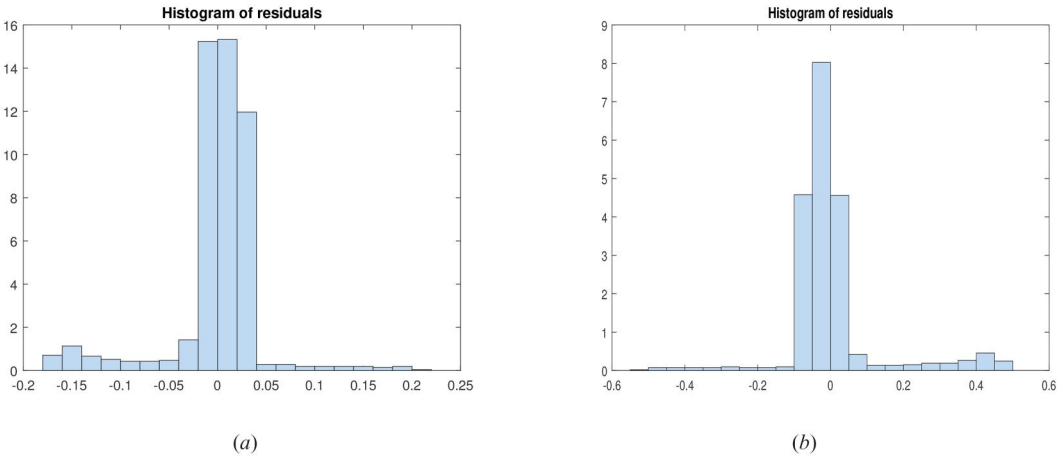


Figure 13. Histogram of residual for skin friction and Nusselt number.

$$\frac{1}{2} Re_x^{\frac{1}{2}} C_{f_{est}} = 0.7682 - 0.00514\gamma - 0.39409M + 0.01230R + 0.001221Pr - 1.0831\Omega - 0.24816H - 0.10445\lambda. \quad (34)$$

$$Re_x^{-\frac{1}{2}} Nu_{x_{est}} = -0.0425 - 0.0607\gamma - 0.07240M + 0.12930R + 0.139256Pr + 0.3856\Omega + 0.2482H + 0.0671\lambda. \quad (35)$$

For skin friction coefficient only γ (independent variable) is not significant and for Nusselt number all the parameters are significant according to [Table 3](#). It is relevant to note that the values of the coefficient of determination or regression coefficient R^2 and the adjusted R-squared (R^2) for both cases are in [Table 2](#). This states clearly that the independent variables fostered a near perfect relationship with the dependent variable SF and NN and the values are 98.69% and 98.76% confidence respectively. Additionally, the variance inflation factor (VIF) is used to assess the strength of correlation between the independent variables as listed in [Table 1](#), both for the skin friction and Nusselt number. However, there is no cause for concern since no multicollinearity or correlation among the independent variables was found for either the skin friction or the Nusselt number.

Table 2. Model summary for skin friction and Nusselt number analysis.

Skin friction (SF)				Nusselt number (NN)			
S	R-sq	R-sq (adj)	R-sq (pred)	S	R-sq	R-sq (adj)	R-sq (pred)
0.0470276	98.69%	98.68%	98.67%	0.126970	98.77%	98.76%	98.76%

Table 3. Linear regression model and parameter estimates for skin friction (SF) and Nusselt number (NN).

Term	Skin friction (SF)					Nusselt number (NN)				
	Coef	SE Coef	T-Value	p-Value	VIF	Coef	SE Coef	T-Value	p-Value	VIF
Constant	0.7682	0.0220	34.85	0.000		-0.0425	0.0595	-0.71	0.475	
γ	-0.00514	0.00507	-1.01	0.311	1.18	-0.0607	0.0137	-4.43	0.000	1.18
M	-0.39409	0.00163	-241.60	0.000	1.18	-0.07240	0.00440	-16.44	0.000	1.18
R	0.01230	0.00195	6.31	0.000	1.18	0.12930	0.00527	24.55	0.000	1.18
Pr	0.001221	0.000194	6.31	0.000	1.18	0.139256	0.000523	266.46	0.000	1.18
Ω	-1.0831	0.0190	-56.95	0.000	1.18	0.3856	0.0513	7.51	0.000	1.18
H	-0.24816	0.00408	-60.85	0.000	1.17	0.2482	0.0110	22.54	0.000	1.18
λ	0.10445	0.00801	-13.04	0.000	1.17	0.0671	0.0216	3.10	0.002	1.17

6. Concluding remark

This study delved into the analysis of a non-similarity solution for the laminar boundary-thermal layer flow problem over a stretching or shrinking sheet with magnetic features and a nonlinear radiation term. The spectral-based numerical technique, particularly the bivariate simple iteration method (BSIM) implemented in MATLAB, was used to solve the coupled multi-variable differential equations. Regression analysis for the skin friction and Nusselt number was conducted to analyze the impact of the response variables. Notably, among the parameters investigated, only the Bingham constant parameter γ exhibited a negligible impact on the skin friction coefficient. Furthermore, all the parameters had a more substantial influence on the Nusselt number. With α set at 0.05, a clear explanation of Tables 1–3 can be provided. Firstly, it is worth noting that the p-value for ANOVA for each of the independent variables corresponds with their counterpart values in the parameter estimates in Table 3. Additionally, if the p-value is less than the α significance level, then the data provides sufficient evidence to conclude that the regression model with the independent variable fits the data better than the model with no independent variable. This implies that we do not have enough evidence to accept the H_0 based on six-parameter model for the skin friction and the seven-parameter model for the Nusselt Number. Two other crucial details are the goodness-of-fit, which is R^2 , and the mean square error, which are considerably small (0.02) for both skin friction and Nusselt number. Moreover, graphical illustrations were used to depict the effects of the fluid parameters of interest, and the results demonstrated that:

- Increasing the streamwise parameter ζ results in an increase in fluid velocity. The practical implication here is that solving the model Eqs. (3)–(5) with its corresponding condition in Eq. (6) in two variables, η and ζ , offers a significant advantage over using η only. The decision to employ the non-similarity transformation is well-justified.
- The magnetic parameter M has an opposing effect on flow over stretching and shrinking sheets for both the velocity and temperature profiles. This implies that the magnetic parameter can act either as an opposing force or a supporting force, depending on the nature of the sheet.
- The radiation parameter R and Prandtl number Pr exhibit opposite behaviors on the velocity and temperature profiles of both the stretching and shrinking sheets. Indeed, the Prandtl number plays a crucial role in influencing how heat is transferred within the fluid. A fluid with a high Prandtl number will exhibit a different temperature profile compared to a fluid with a low Prandtl number. This difference arises because the ratio of thermal to momentum

diffusivity, inherent in the Prandtl number, influences the thermal boundary layer thickness and heat transfer rates.




- The Newtonian fluid serves as the turning point for both shear thickening and shear thinning in terms of skin drag and Nusselt number. This indeed suggests that for a specific value of the Reiner-Philippoff fluid parameter λ , the fluid exhibits behavior characteristic of shear-thickening, Newtonian, or shear-thinning fluid, respectively.

Exploring the potential of using spectral-based iterative numerical method to effectively handle the nonlinearity arising from the shear stress-shear rate relationship in the Reiner-Philippoff fluid, and investigating the existence of dual/multiple solutions through the introduction of nanoparticles, could lead to valuable insights. We will investigate this in future studies.

Disclosure statement

The authors read and approved the article, in addition declared no conflict of interest.

ORCID

Yusuf O. Tijani  <http://orcid.org/0000-0002-9127-7173>
 Shina D. Olonijun  <http://orcid.org/0000-0002-9794-8580>
 Olumuyiwa Otegbeye  <http://orcid.org/0000-0003-1321-9776>
 Ajiboye R. Babalola  <http://orcid.org/0000-0001-7718-5160>

References

- [1] T. Y. Na, "Boundary layer flow of Reiner-Philippoff fluids," *Int. J. Non Linear Mech.*, vol. 29, no. 6, pp. 871–877, 1994. DOI: [10.1016/0020-7462\(94\)90059-0](https://doi.org/10.1016/0020-7462(94)90059-0).
- [2] Y. O. Tijani, A. T. Adeosun, H. A. Ogunseye, and H. Niranjana, "Magnetic dipole dynamics on Reiner-Philippoff boundary layer flow," *Numer. Heat Transf. A Appl.*, pp. 1–15, 2023. DOI: [10.1080/10407782.2023.2209925](https://doi.org/10.1080/10407782.2023.2209925).
- [3] K. G. Kumar, M. G. Reddy, M. I. Khan, F. Alzahrani, M. I. Khan, and E. R. El-Zahar, "Heat transfer and melting flow of a Reiner-Philippoff fluid over a surface with Darcy-Forchheimer medium," *Case Stud. Therm. Eng.*, vol. 28, pp. 101649, 2021. DOI: [10.1016/j.csite.2021.101649](https://doi.org/10.1016/j.csite.2021.101649).
- [4] Y. O. Tijani, M. T. Akolade, K. B. Kasali, and H. A. Ogunseye, "Dynamics of carbon nanotubes on Reiner-Philippoff fluid flow over a stretchable rigid plate," *Ind. J. Phys.*, 2023. DOI: [10.1007/s12648-023-02872-z](https://doi.org/10.1007/s12648-023-02872-z).
- [5] T. Hayat, M. Rafiq, and B. Ahmad, "Soret and DuFour effects on MHD peristaltic flow of Jeffrey fluid in a rotating system with porous medium," *PLoS One*, vol. 11, no. 1, pp. e0145525, 2016. DOI: [10.1371/journal.pone.0145525](https://doi.org/10.1371/journal.pone.0145525).
- [6] T. Hayat, A. Shafiq, A. Alsaedi, and S. Asghar, "Effect of inclined magnetic field in flow of third grade fluid with variable thermal conductivity," *AIP Adv.*, vol. 5, pp. 087108, 2015.
- [7] F. Mabood, W. A. Khan, and A. I. M. Ismail, "MHD flow over exponential radiating stretching sheet using homotopy analysis method," *J. King Saud Univ. Eng. Sci.*, vol. 29, no. 1, pp. 68–74, 2017. DOI: [10.1016/j.jksues.2014.06.001](https://doi.org/10.1016/j.jksues.2014.06.001).
- [8] G. T. Thammanna, K. G. Kumar, B. J. Gireesha, G. K. Ramesh, and B. C. Prasannakumara, "Three dimensional MHD flow of couple stress Casson fluid past an unsteady stretching surface with chemical reaction," *Results Phys.*, vol. 7, pp. 4104–4110, 2017. DOI: [10.1016/j.rinp.2017.10.016](https://doi.org/10.1016/j.rinp.2017.10.016).
- [9] D. G. Prakasha, M. V. V. N. L. Sudharani, K. G. Kumar, E. M. Elsaid, and M. R. Eid, "Thermal amelioration of aluminium nano-alloys on swirling aqueous MHD viscous nanofluid flow via a deformable cylinder: applying magnetic dipole," *J. Therm. Anal. Calorim.*, vol. 148, no. 13, pp. 6197–6206, 2023. DOI: [10.1007/s10973-023-12130-3](https://doi.org/10.1007/s10973-023-12130-3).
- [10] D. H. Babu, K. K. Naidu, S. Deo, and P. V. S. Narayana, "Impacts of inclined Lorentz forces on hybrid CNTs over an exponentially stretching sheet with slip flow," *Int. J. Model. Simul.*, vol. 43, no. 3, pp. 310–324, 2022. DOI: [10.1080/02286203.2022.2079109](https://doi.org/10.1080/02286203.2022.2079109).
- [11] I. Swain, S. R. Mishra, and H. B. Pattanayak, "Flow over exponentially stretching sheet through porous medium with heat source/sink," *J. Eng.*, vol. 2015, pp. 1–7, 2015. DOI: [10.1155/2015/452592](https://doi.org/10.1155/2015/452592).

- [12] A. Hussain, S. Afzal, R. Rizwana, and M. Y. Malik, “MHD stagnation point flow of a Casson fluid with variable viscosity flowing past an extending/shrinking sheet with slip effects,” *Phy. A.*, vol. 553, pp. 125080, 2020.
- [13] Y. O. Tijani, S. D. Olonijiu, K. B. Kasali, and M. T. Akolade, “Nonsimilar solution of a boundary layer flow of a Reiner–Philippoff fluid with nonlinear thermal convection,” *Heat Trans.*, vol. 51, no. 6, pp. 5659–5678, 2021. DOI: [10.1002/htj.22564](https://doi.org/10.1002/htj.22564).
- [14] S. Jeevitha, M. Chitra, and B. R. Kumar, “MHD flow in a rotating vertical cone through a porous medium,” *Heat Trans.*, vol. 52, no. 3, pp. 2165–2185, 2023. DOI: [10.1002/htj.22779](https://doi.org/10.1002/htj.22779).
- [15] G. Kumaran, N. Sandeep, and I. L. Animasaun, “Computational modeling of magnetohydrodynamic non-Newtonian fluid flow past a paraboloid of revolution,” *Alex. Eng. J.*, vol. 57, no. 3, pp. 1859–1865, 2018. DOI: [10.1016/j.aej.2017.03.019](https://doi.org/10.1016/j.aej.2017.03.019).
- [16] S. Lun Hung and J. Leong, “Effects of regional magnetic field on rotating MHD flow field of unity magnetic Prandtl number,” *J. Appl. Math.*, vol. 2012, no. 6, pp. 1–17, 2012. DOI: [10.1155/2012/804105](https://doi.org/10.1155/2012/804105).
- [17] S. S. Motsa, “A new spectral local linearization method for nonlinear boundary layer flow problems,” *J. Appl. Math.*, vol. 2013, pp. 1–15, 2013. DOI: [10.1155/2013/423628](https://doi.org/10.1155/2013/423628).
- [18] S. S. Motsa, “On the practical use of the spectral homotopy analysis method and local linearisation method for unsteady boundary-layer flows caused by an impulsively stretching plate,” *Numer. Algor.*, vol. 66, no. 4, pp. 865–883, 2014. DOI: [10.1007/s11075-013-9766-z](https://doi.org/10.1007/s11075-013-9766-z).
- [19] S. S. Motsa, P. G. Dlamini, and M. Khumalo, “Spectral relaxation method and spectral quasilinearization method for solving unsteady boundary layer flow problems,” *Adv. Math. Phys.*, vol. 2014, pp. 1–12, 2014. DOI: [10.1155/2014/341964](https://doi.org/10.1155/2014/341964).
- [20] S. S. Motsa, V. M. Magagula, and P. Sibanda, “A bivariate Chebyshev spectral collocation quasilinearization method for nonlinear evolution parabolic equations,” *Sci. World J.*, vol. 2014, pp. 581987, 2014. DOI: [10.1155/2014/581987](https://doi.org/10.1155/2014/581987).
- [21] H. A. Ogunseye, S. O. Salawu, Y. O. Tijani, M. Riliwan, and P. Sibanda, “Dynamical analysis of hydromagnetic Brownian and thermophoresis effects of squeezing Eyring–Powell nanofluid flow with variable thermal conductivity and chemical reaction,” *MMMS*, vol. 15, no. 6, pp. 1100–1120, 2019. DOI: [10.1108/MMMS-01-2019-0008](https://doi.org/10.1108/MMMS-01-2019-0008).
- [22] M. T. Akolade and Y. O. Tijani, “A comparative study of three dimensional flow of Casson–Williamson nanofluids past a rigid plate: spectral quasi-linearization approach,” *Partial Differ. Eq. Appl. Math.*, vol. 4, pp. 100108, 2021. DOI: [10.1016/j.padiff.2021.100108](https://doi.org/10.1016/j.padiff.2021.100108).
- [23] V. M. Magagula, “On the multidomain bivariate spectral local linearisation method for solving systems of nonsimilar boundary layer partial differential equations,” *Int. J. Math. Math. Sci.*, vol. 2019, pp. 1–18, 2019. DOI: [10.1155/2019/6423294](https://doi.org/10.1155/2019/6423294).
- [24] A. Shahid, H. L. Huang, C. M. Khalique, and E. Bhatti, “Numerical analysis of activation energy on MHD nanofluid flow with exponential temperature-dependent viscosity past a porous plate,” *J. Therm. Anal. Calorim.*, vol. 143, no. 3, pp. 2585–2596, 2020. DOI: [10.1007/s10973-020-10295-9](https://doi.org/10.1007/s10973-020-10295-9).
- [25] A. S. Idowu and B. O. Falodun, “Soret–dufour effects on MHD heat and mass transfer of Walter’s-b viscoelastic fluid over a semi-infinite vertical plate: spectral relaxation analysis,” *J. Taibah Univ. Sci.*, vol. 13, no. 1, pp. 49–62, 2019. DOI: [10.1080/16583655.2018.1523527](https://doi.org/10.1080/16583655.2018.1523527).
- [26] S. Shateyi and H. Musara, “On the numerical analysis of unsteady MHD boundary layer flow of Williamson fluid over a stretching sheet and heat and mass transfers,” *Computation*, vol. 8, no. 2, pp. 55, 2020. DOI: [10.3390/computation8020055](https://doi.org/10.3390/computation8020055).
- [27] N. Rai and S. Mondal, “Spectral methods to solve nonlinear problems: a review,” *Partial Differ. Equ. Appl. Math.*, vol. 4, pp. 100043, 2021. DOI: [10.1016/j.padiff.2021.100043](https://doi.org/10.1016/j.padiff.2021.100043).
- [28] O. Otegbeye, S. P. Goqo, and M. S. Ansari, “Comparative study of some spectral based methods for solving boundary layer flow problems,” *AIP Conf. Proc.*, vol. 2253, pp. 020013, 2020.
- [29] S. S. Motsa, V. Magagula, and Z. Makukula, “Simple iteration method(s) for nonlinear differential equations: theory and development,” 10th Annual Research Workshop on Numerical Methods for Differential Equations, University of KwaZulu-Natal, Pietermaritzburg Campus, 2017.
- [30] L. N. Trefethen, *Spectral Methods in MATLAB*, SIAM, vol. 10, 2000.